Pion production excitation functions in proton-nucleus collisions from the absolute threshold to 500 MeV

J. Mårtensson,[1] M. Berg,[1] L. Carlén,[1] R. Elmér,[1] A. Fokin,[1] R. Ghetti,[1] B. Jakobsson,[1] B. Norén,[1] A. Oskarsson,[1] H. J. Whitlow,[1] C. Ekström,[2] G. Ericsson,[2] J. Romanski,[2] E. J. van Veldhuizen,[2] L. Westerberg,[2] J. Julien,[3] K. Nybö,[4] T. F. Thorsteinsen,[4,*] S. Amirelmi,[4] M. Guttormsen,[5] G. Løvhøiden,[5] V. Bellini,[6] F. Palazzolo,[6] M. L. Sperduto,[6] C. Sutera,[6] V. Avdeichikov,[7,1] A. Kuznetsov,[8,2] and Yu. Murin[8]

(CHIC Collaboration)

[1]*Department of Physics, University of Lund, Lund, Sweden*
[2]*The Svedberg Laboratory and Department of Neutron Physics, University of Uppsala, Uppsala, Sweden*
[3]*Centre d'Etudes Nucléaires, Saclay, France*
[4]*Department of Physics, University of Bergen, Bergen, Norway*
[5]*Department of Physics, University of Oslo, Oslo, Norway*
[6]*INFN/LNS, University of Catania, Catania, Italy*
[7]*Joint Institute for Nuclear Research, Dubna, Russia*
[8]*V. G. Khlopin Radium Institute, St. Petersburg, Russia*

(Received 31 March 1999; revised manuscript received 2 February 2000; published 19 June 2000)

Pion excitation functions in proton-nucleus collisions, from the absolute threshold to 500 MeV, have been measured with 1 MeV beam energy resolution at the CELSIUS storage ring, operating in slow ramping mode. Total yields, angular distributions, and target mass dependence of π^+ production are generally reproduced well by QMD calculations. The π^+/π^- ratios are not reproduced equally well, obviously because the detailed description of the pion interaction with the Coulomb field is very delicate.

PACS number(s): 25.40.Ve, 24.10.Nz, 25.70.−z

I. INTRODUCTION

The threshold energy (E_{th}) for (charged) pion production, which is 289 MeV in free nucleon-nucleon (NN) collisions, decreases substantially in nucleon-nucleus collisions due to the Fermi boost [1] or collective (multinucleon) interaction. Actually, a normal ground state Fermi momentum of 260 MeV/c in, e.g., a Kr nucleus reduces the threshold for pion production in (off-shell) NN collisions, almost to the fully collective $p+{}^{84}$Kr threshold, which is $\sim$141 MeV.

The description of NN interactions in both mean-field and cascade models is well established, and it is therefore hardly surprising that such models describe the gross features of pion production at energies around and above the free NN threshold quite well. However, at lower energies, in the so-called subthreshold region, details of pion and Coulomb potentials as well as reabsorption properties are so delicate that it is a much harder task to describe existing data. On the other hand, only first-chance nucleon-induced collisions contribute and there were serious attempts already in the 1970s by Sternheim and Silbar [2] to prescribe pion production over a wide range of energies by the coherent isobar model which were quite successful in describing data [3]. Very close to the fully collective threshold even nuclear structure starts to play an important role, and individual excited states of the target nucleus are probed rather than its average ground state properties. In nucleus-nucleus collisions this is even more stressed, and one has, e.g., clearly observed coherent excitation of the delta resonance in the energy transfer spectra of (^{3}He,t), (^{20}Ne,^{20}Na), or (^{20}Ne,^{20}F) reactions [4]. Even if these results show that peripheral, surfacelike, reactions favor pion production at higher energies, it is obvious that central collisions must dominate it in the subthreshold region not only because of the double Fermi boost but also possibly because of compression, at least in reactions between heavy nuclei [5]. A thorough review of threshold phenomena in nucleus-nucleus collisions is presented in Ref. [6].

In our first attempts to utilize the CELSIUS storage ring for measuring π^+ yields with a continuously increasing beam energy we studied both p-nucleus and nucleus-nucleus collisions. The power of these excitation function data was demonstrated in Ref. [7]. In the present paper we present more complete data on total yields, differential cross sections, angular distributions, and target mass dependence of π^+ production in $p+$N, Ar, Kr, Xe reactions and on π^+/π^- ratios in $p+$Kr reactions from a series of experiments where the bombarding proton beam has an energy from below the absolute pion production threshold up to 500 MeV. Even though there exist data on both charged and neutral pion production at a number of beam energies, it is obvious that such excitation function data can set much stronger constraints on the proposed models. The different gas-jet targets that were utilized make it possible to study the importance of collective phenomena, and the fact that we were able to collect data on both π^+ and π^- makes it possible to set constraints on the Coulomb field. Similar slow ramping experiments on π^0 production would strengthen these conclusions on Coulomb effects, and also make it possible to study, e.g., the validity in detail of the isospin decomposition when comparing data to any NN-based model. Comparisons to results

*Deceased.

from cascade models [8,9] and Boltzmann-Uehling-Uhlenbeck (BUU) models [7,10] have already been presented, and in this paper we concentrate instead our comparisons with theory first on a simple available phase-space estimate and then on a detailed, mean-field+NN, QMD model.

II. EXPERIMENT

A. Celsius storage ring

The internal PIG source produces an H_2^+ beam with an electrical current up to 10e μA which is accelerated in the Gustaf Werner Cyclotron (GWC) to 96 MeV and then transported to the CELSIUS storage ring [11] where it is introduced by stripping injection. About 1×10^{11} protons are typically stored in the CELSIUS ring. The beams can be accelerated up to energies of 1.36 GeV (protons) or 470A MeV ($Z/A=1/2$). Electron cooling for beams with velocities corresponding to an electron energy of 300 keV is possible. No cooling is, however, used in the slow ramping experiments discussed in this paper.

The cluster gas-jet target [12] is able to produce a cluster density in the target area with a thickness up to 1×10^{14} atoms/cm^2 for light gases (N,Ne) and 2×10^{13} atoms/cm^2 for heavy gases (Xe). These target fluxes give typical half-lives of the proton beam from 1 to 5 min. The beam lifetime depends strongly on the energy. After the injection phase, the beam is accelerated to the start energy for the data taking. At this moment the gas jet is switched on, and the beam energy is continuously increased by slow ramping of the magnets. In the very first experiment of this kind [7], we utilized two (overlapping) ramp cycles covering beam energies of 170–270 MeV and 250–500 MeV. In the second experiment, we used only one wider ramp covering 150–500 MeV. A typical ramp cycle lasts for 250 s; then the gas-jet is switched off, the beam is dumped, and a new cycle starts with proton injection (Fig. 1). The cycles, chosen in our experiments, were 300 s long, except for the low energy cycles with Kr and Xe targets, where 120 s cycles were used since we always required that $\geqslant1/3$ of the stored protons should remain at the end of the cycle.

The luminosity $L=\nu\times\phi\times t\times f$ varied between 10^{30} and 10^{31} cm^{-2} s^{-1}. Here ν is the frequency, ϕ is the number of stored protons, t is the target thickness, and f accounts for the effective gas-jet/beam overlap. The beam energy in each event is obtained by starting a clock in the data acquisition (DAQ) at $t=t_{start}$ (see Fig. 1) and the time is then read out when an event trigger is obtained. The event time (t_{event}) is then translated to beam energy via the frequency (ν) table of the cycle, monitored continuously in the accelerator control. The individual collision energy is

$$E_{event}(\nu)=\left(\frac{1}{\sqrt{1-(\nu s/c)^2}}-1\right)M, \qquad (1)$$

where $s=81.8$ m is the circumference of the storage ring and M is the mass of the beam particle.

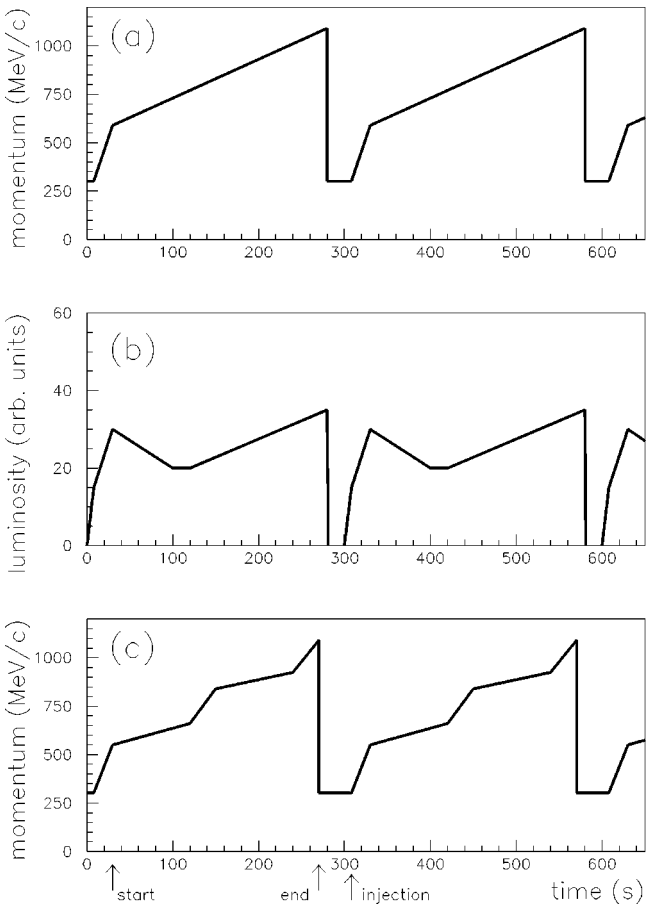

FIG. 1. Principle sketch of the beam momentum cycle (a), the luminosity variation (b), and the specific beam momentum cycle utilized in the second experiment (c).

The high accuracy in the frequency determination and the good reproducibility of the ramping cycle make the precision in the event momentum determination quite high, $\Delta p/p\sim1.5\times10^{-3}$. In the first experiment [Fig. 1(a)] a linear p_{beam}-time relation was used, whereas in the second experiment we operated with three different dp/dt gradients in order to assure collection of large enough statistics in regions of special interest [Fig. 1(c)]. The first region of interest that is indicated in Fig. 1(c) is close to the absolute threshold and the second region is the one where narrow resonances in the pion production have been reported [13,14]. Actually it turned out that almost any forms of ramp cycles can be created at CELSIUS and reproduced with high precision.

B. Range telescopes

Five (NE102) plastic scintillator range telescopes were installed to detect charged pions [15]. The telescopes were placed at 20°, 55°, 75°, 97°, and 120° in the first experiment and in the second experiment at 20°, 55°, 75°, 90°, and 150°. Each telescope consists of ten detectors, the last one operating in veto mode. The individual detector thicknesses are chosen to cover approximately equal (~8 MeV) energy bins. The energy signals are digitized with 10-bit analog-to-digital converters (ADC's), and if

needed, proper response functions could be achieved which would give higher pion energy resolution. We have, however, chosen to keep the 8 MeV binning since it gives reasonable statistics for pion energy spectra when 1 MeV beam energy binning is introduced. It should be stressed that this rough pion energy binning does not affect any $p-\pi$ or $\pi^+ - \pi^-$ separation. Coincident signals from the first three detectors form the trigger. All pions that stop in detectors 3–9 are included in the data. According to thicknesses and range-energy tables, this corresponds to energy intervals of 11–60 MeV in the 20° telescope, 11–84 MeV in the 55° and 75° telescopes and 16–75 MeV (expt. 1) or 15–75 MeV (expt. 2) in the 97° or 90° and backward telescopes. The first three detectors were separated by several cm in order to get good enough directional sensitivity to avoid background from particles not produced in the beam-target overlap volume. Philips XP 2020 photomultiplier (PM) tubes were used to read out all detectors except those in the forward telescope, where the limited space required 3/4″ tubes (Hamamatsu R1166).

This kind of range telescopes has proved earlier to be a powerful instrument for subthreshold charged pion studies, especially for π^+ [15–17]. The main advantages are (i) fast signals allow operation at high countrates, (ii) good discrimination of π^+ vs π^- and very good discrimination against all other singly charged particles, and (iii) provision of a powerful hardware trigger for pions.

C. Electronics

A block scheme of the readout electronics is shown in Fig. 2. The pion trigger requires a coincidence between the first three detectors in a telescope, each producing a signal above a discriminator level of ~30 mV. The coincidence overlap time for this trigger was set to 30 ns. All signals in detectors 1–7 are also compared to a second, high discriminator threshold. A veto is created if any signal in detectors $1,\ldots,S-2$ (S stands for stop detector) is above this level. This gives a direct, hardware rejection against protons and heavier particles. As a result of this rejection, the data collection could be performed at a rate nearly matching the maximum luminosity. The whole logic chain is produced in about 100 ns, and the analog signals for the ADCs have to be delayed by the same time in order to have the gate signal arriving 10 ns before. If the particle has not been rejected at this stage, a trigger is sent to open the ADC gates, unless the CAMAC readout system is busy and vetoes the new event. The detector where the pion comes to rest (the stop detector) is determined by a pattern unit which sets one bit for each detector in which there is a signal exceeding the 30 mV discriminator level.

D. Pion identification

In order to separate π^+ from π^- each analog signal is integrated in two different (charge sensitive) ADCs with individually adjusted gates (Fig. 2). The first gate is ~100 ns long and opens the ADC~10 ns before the maximum of the analog pulse appears. The rise time of the signal from the (XP 2020) PM tube is 6–7 ns and the second gate, ~90 ns long, opens another ADC shortly after the maximum. For

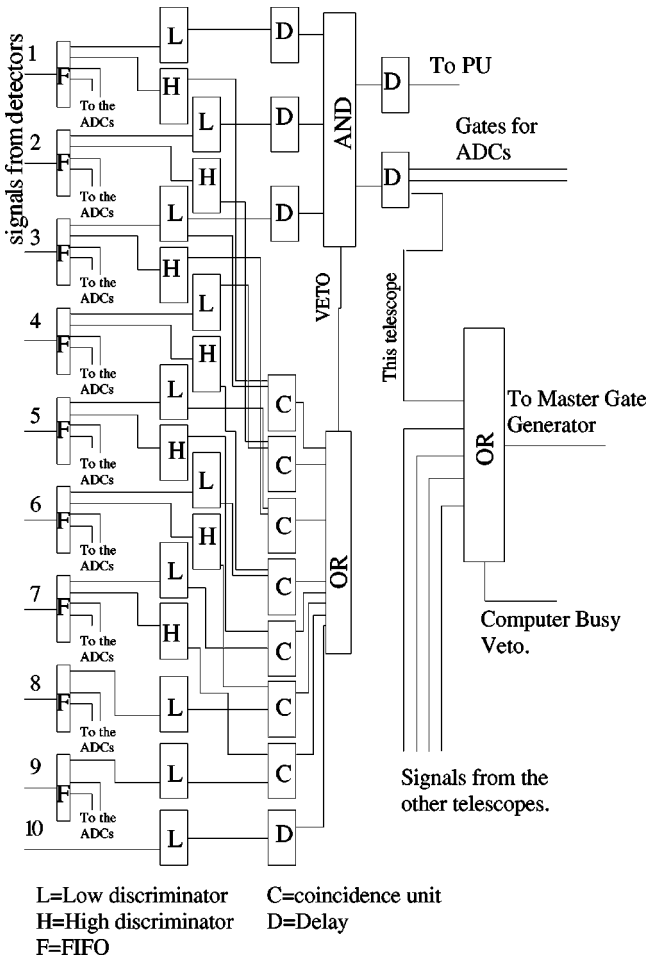

FIG. 2. Block scheme for electronics.

each event trigger these two ADC values and the event time are stored by the (VME) DAQ system. Typical correlations between the prompt S and $S-1$ signals come out as in Fig. 3(a) when the stop detector is the sixth one. When the prompt stop signal is plotted versus the delayed one, separation between π^+ and π^- is obtained due to the additional muon energy signal from the $\pi^+ \rightarrow \mu^+ \nu$ decay with a lifetime of 26 ns [Fig. 3(c)]. A stopping π^- is absorbed by a nucleus in the detector material and therefore no extra muon signal is obtained in this case. The separation is quite good but there is of course a certain efficiency in this method due to the fact that in some cases only a part of the (monoenergetic) 4.2 MeV muon energy is delivered to the stop detector (see also Sec. II E 1). However, the π^- absorption creates the problem that charged decay products from the excited detector nucleus will add up to the total integrated signal and such distorted correlations can be observed particularly in Figs. 3(b) and 3(c). Because of this, it is not possible to use the $\Delta E - E$ correlation plot to identify charged pions. Instead the sum of π^+ and π^- has to be identified from the ΔE signals in the $1,\ldots,S-1$ detectors (in this example $S-1=5$). The remaining proton contamination is small in this case. A pion which stops in detector 3 will have only one $\Delta E - \Delta E$ correlation for its identification whereas a pion that stops in detector 9 has seven possible correlations to utilize,

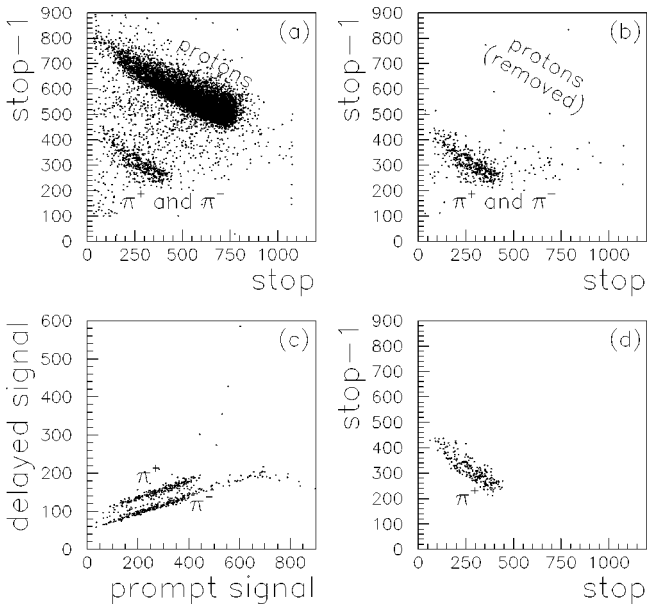

FIG. 3. (a) $\Delta E-E$ (signal amplitude) correlation without proton rejection. (b) Protons have been removed by cuts in the preceding $\Delta E-\Delta E$ correlations. (c) Prompt signal-delayed signal correlation after proton removal. (d) $\Delta E-E$ correlation after π^+ selection in (c). All numbers refer to ADC channel numbers.

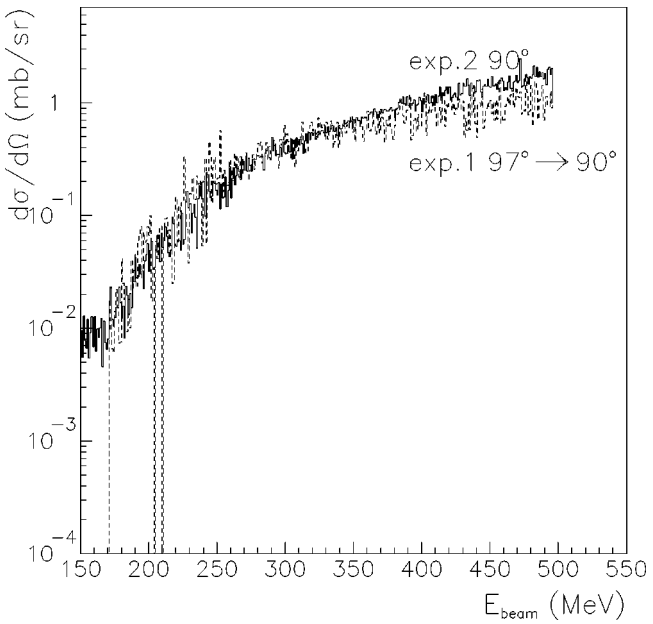

FIG. 4. Comparison between differential, $d\sigma/d\Omega$, cross sections of π^+ at 90° in $p+\mathrm{Kr}$ collisions measured in experiments 1 and 2.

which of course creates some difference in the error of the determined charged pion number (Sec. II E 2). Finally we explore in Fig. 3(d) a typical $\Delta E-E$ correlation plot after both protons and π^- (in the prompt-delayed plot) have been removed.

In order to correct for the loss of pions due to scattering, absorption, and decay, efficiency factors are introduced when estimating the total number of pions (see Sec. II E 1).

E. Normalization, statistical, and systematic errors

1. Normalization

The number of stored ions is decreasing during the beam cycle, due to losses in the target and rest gas, but as the frequency increases during acceleration the luminosity may still increase [see Fig. 1(b)]. The absolute luminosity, which depends on the beam intensity, target gas flow, and the overlap between beam and target, could not be measured directly. Therefore, an absolute normalization monitor telescope is used. High-energy (52–161 MeV) protons emitted at 97° or 90° (second experiment) were thereby registered in a standard range telescope. The production cross sections for these protons were calculated by a standard BUU code [10] and if necessary and/or possible the absolute level was adjusted from empirical information [18,19]. Since on-line proton rejection (see Sec. II C) was introduced in all pion telescopes in the first experiment, special calibration runs were performed to control the proton rejection efficiency. This was done by setting up two identical telescopes at the same angle, 97°, one acting as an ordinary monitor/pion telescope and the other one with the proton rejection removed. In the second experiment a prescaler was installed which allowed 1/16 of the events to be registered without proton rejection. The pion cross sections are thus given in the first experiment by

$$\frac{d\sigma_\pi}{d\Omega}=f_{eff}\frac{N_\pi}{N_p}\Delta\Omega\left(\frac{N^c_{\pi nr}}{N^c_{\pi r}}\frac{N^c_{pr}}{N^c_{pnr}}\right)\int_{52}^{161}\frac{d^2\sigma_p}{d\Omega dE}dE \qquad (2)$$

and in the second experiment by a simpler formula

$$\frac{d\sigma_\pi}{d\Omega}=f_{eff}\frac{N_\pi}{N_p}\Delta\Omega\frac{1}{16}\int_{52}^{161}\frac{d^2\sigma_p}{d\Omega dE}dE. \qquad (3)$$

f_{eff} is here an efficiency factor which corrects for pion decay in flight (also during slow down in the detector material) and for pion-nucleus collisions in the detector material [17,20]. For π^+ it also accounts for the efficiency in the prompt/delay ADC signal identification method [21]. $\Delta\Omega$ corrects for (eventual) differences between the solid angles of the monitor telescope and the telescope in which the pions are registered. N_π/N_p is the registered pion to proton ratio which is corrected either from the special normalization run (denoted c) through the expression within brackets in (2) (r stands for rejected and nr for nonrejected particles) or through the prescaling factor 1/16 in Eq. (3). The integral term is the proton cross section for the monitor telescope. Thus the only difference in determining $d\sigma_\pi/d\Omega$ in the two experiments lies in the correction term. Since the emission of pions at 55° and 75° from $p+\mathrm{Kr}$ reactions has been measured in both experiments, and furthermore a modest extrapolation from a 97° to 90° differential cross section in the data from the first experiment can be performed easily, we can compare data from the two normalization methods. Some difference was found only in the high-beam-energy region which made us correct all data from the first experiment. Further details about this are given in Sec. III A and Fig. 4.

2. Systematic errors

Based on comparisons between overlapping data taken both with low- and high energy ramps in the first experiment and on comparisons between $p+\mathrm{Kr}$ data from the first experiment and the second (single ramp) experiment, we estimate the uncertainty in the determined N_π/N_p ratio to be at most 20%. The latter comparison is exploited in Fig. 4. Other systematic errors, mainly coming from the correction factors, are similar for the two experiments. Computer dead-time and luminosity variations do not contribute to the errors due to the fact that we use ratios between yields of two kinds of particles, registered under identical conditions. The loss of π^+ in the analysis is connected to the resolution in the delayed-prompt method which depends on how accurate the gate setting is made for the pulse shape analysis. Delaying the start of the second ADC gate improves the π^+/π^- resolution but then the π^+ efficiency decreases because of the increasing number of pions that decay before the delayed gate is opened.

The efficiency of the muon registration has been measured directly for the backward $(97°,120°)$ telescopes [21] to be 90%. Monte Carlo calculations give efficiencies for the $55°$ and $75°$ telescopes of 82% and for the $20°$ telescope to 77%. The differences come essentially from the different geometries of the telescopes. The corrections for pion decay in flight, setup geometry, and scattering of pions give a total systematic uncertainty of 15%. A systematic error of 4% arises because of the uncertainty in the solid angles of the different detectors. The BUU calculations for the proton cross section introduce a systematic error of 20%. In the first experiment, an additional 12% systematic error is estimated for the efficiency calibration of the proton monitor. The efficiency in the pion selection process of the data analysis contributes to the systematic error with 7% for those stopping in detector 3 and 2% for those stopping in detector 9.

When integrating double differential cross sections, to get total yields of pions, we extrapolate the pion energy distribution both below and above the energy range of the telescopes. These extrapolations were determined by the normalized BUU calculations which were also used to interpolate between the measured angles in order to perform $d\sigma/d\Omega$ integration. The uncertainties in these estimations contribute with 20% to the systematic error of the absolute pion cross section.

All systematic uncertainties add up to a total error of 35%, except for the lowest beam energies, very close to the absolute pion production threshold. Here, the total error is $\sim 50\%$, mainly because of an increasing uncertainty in the estimated proton cross sections and to the determination of the general (flat) background in the π/p ratio which is important only here (see Sec. III A and Fig. 4). The estimation of the systematic errors seems well confirmed by comparisons to earlier data, obtained in fixed-target experiments (see next section). Because of the complicated absolute normalization procedure, the systematic errors are thus larger than in conventional experiments, where they are often reported to be between 20% and 30%. Most of the conclusions we draw in this paper are not affected seriously by this fact but in those cases where it may be a problem we will discuss it specifically.

TABLE I. List of data sets.

Reaction	Angular position	Beam energy	Comment
$p+\mathrm{N}$	$55°$, $75°$, $97°$, $120°$	169–500 MeV	expt. 1
$p+\mathrm{Ar}$	$55°$, $75°$, $97°$, $120°$	169–500 MeV	expt. 1
$p+\mathrm{Kr}$	$55°$, $75°$, $97°$, $120°$	169–500 MeV	expt. 1
$p+\mathrm{Kr}$	$20°$, $55°$, $75°$, $90°$, $150°$	150–500 MeV	expt. 2
$p+\mathrm{Xe}$	$55°$, $75°$, $97°$, $120°$	169–500 MeV	expt. 1

3. Statistical errors

The statistical errors have contributions from both pions and protons since the ratio between the yields of these particles are introduced in Eqs. (2) and (3). The contribution to the error from protons is, however, nearly negligible. The statistical errors are presented in the figures only for a few points as typical examples. Normally the statistical fluctuations are easy to recognize in the excitation function figures.

III. EXPERIMENTAL RESULTS

A. π^+ production cross sections

Table I presents the list of data sets to be discussed in this section. The differences between experiments 1 and 2 are explained in the previous section. It must be noticed that data in expt. 1 were collected in two parts, with a low-beam-energy ramp, 169–270 MeV, and a high-energy ramp, 250–500 MeV. In expt. 2, all data were collected in one single ramp covering the energy interval 150–500 MeV.

In Fig. 4, the absolute differential cross section $d\sigma/d\Omega$ of 16–75 MeV π^+ emitted at $90°$ in $p+\mathrm{Kr}$ reactions is presented from the two different experiments. An extrapolation of expt. 1 data from $97°$ to $90°$ has been made but this should affect the result very little since the angular dependence is very smooth at these angles. Actually, the $55°$ and $75°$ data were obtained at the same angles in the two experiments but the statistics are lower so it is assumed that the $90°$ data sets are the most proper ones for eventual normalization. A slightly stronger beam energy dependence in the data of expt. 2 is found in the region of the high-energy ramp. The comparison in the region of the low-energy ramp shows very good agreement. The $55°$ and $75°$ data confirm these tendencies. The most plausible explanation for the difference at high beam energies is that there is a difference in the absolute normalizing procedure, which is simpler and more reliable in expt. 2. Even if all data agree within the systematic errors (see [7] and Sec. II E 2 above) we therefore renormalize all data from expt. 1 by the beam-energy-dependent ratio $R_{12}(E_{beam})$, determined from the data of Fig. 4.

The discussion in Sec. II E 1 of corrections introduced to obtain absolute cross sections omitted the eventual remaining background after all conditions on the ADC signals have been set. Thus the data in Fig. 4 still contain ''random'' background of this kind. Since the data taken in this case

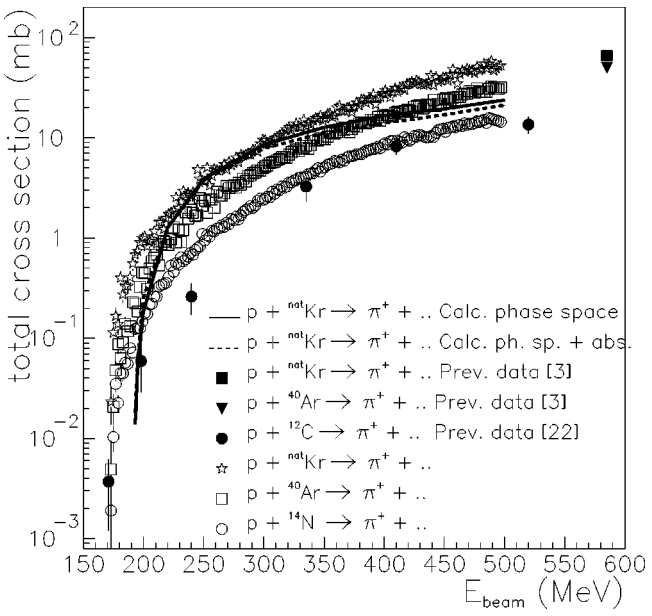

FIG. 5. The total cross section of π^+ from $p+\mathrm{N}$, $p+\mathrm{Ar}$, and $p+\mathrm{Kr}$ collisions. Previous data points and available phase-space calculations (curves) are further discussed in the text.

even extend to beam energies below the absolute threshold for producing a 16 MeV pion at 90°, it confirms that there is such a background. Further investigations of this background for pions with higher energies, i.e., those stopping deeper down into the telescope, thereby moving the production threshold to higher beam energy (e.g., to 182 MeV for pions that stop in, or after, detector 7), confirms this background and indicates that it has a weak beam energy dependence. This ''random'' background must be related to uncorrelated particles from the beam halo hitting material far away from the target position since our directional sensitivity towards the beam/target interaction point is quite high. It should be stressed that this background is important only close to the absolute threshold, say, below 200 MeV, even if some increase with increasing beam energy might appear. In expt. 1 it is difficult to set this background level in the data representing pions that stop in detector 3 due to the fact that the absolute threshold is lower than the experimental cutoff of 169 MeV. Therefore the signal/background ratios are determined from stop detectors 4–8 only and the same ratio is used for stop detector 3. In all subsequent figures this ''random'' background has been subtracted.

Figure 5 shows the total cross section of π^+ in $p+{}^{14}\mathrm{N}$, $p+{}^{40}\mathrm{Ar}$, and $p+{}^{nat}\mathrm{Kr}$ reactions. Other data for reactions as close as possible to those measured in this experiment that were found in the literature [22] are shown for comparison. To obtain total yields from our data, the differential cross sections have been extrapolated below and above the experimental cutoff. We use the method described in [7] which is based on theoretical predictions with additional absolute normalization to data in the measured energy region. The angular dependence is finally described by $d\sigma/d\Omega = a\cos^2\Theta + b\cos\Theta + c$ with a (beam energy-dependent) set of a, b, and c parameters obtained in least squares fits. This form of the angular dependence is actually suggested by the standard BUU calculations which we used again to confirm the extrapolations.

The comparison to previous data shows in general good agreement (Fig. 5) except in the subthreshold region where in one point up to a factor of 2.5 times larger yield is obtained in our experiment. We stress that the target mass difference ($p+\mathrm{C}$ compared to $p+\mathrm{N}$) is responsible for $\sim 20\%$ of the difference in the deep subthreshold region ($\sim 10\%$ in the high-energy region) and that the systematic errors are here as large as up to 50% and 30%, respectively. Statistical errors of the order of 20% are reported for the spectrometer experiments. This means that up to about a factor of 2 difference would be acceptable as nonsignificant in single points. Thus we must conclude that in the region 200–300 MeV we do obtain significantly larger total cross sections of π^+ than reported earlier [22], although the agreement is very good both at higher and lower energies.

The $p+\mathrm{Ar}$ and $p+\mathrm{Kr}$ cross sections can only be compared to one single experiment above the measured range, at 585 MeV [3], which, however, compares well to a reasonable extrapolation of our data. For $p+\mathrm{Kr}$ we also present the expected increase of the cross section with increasing beam energy if just the available phase space is considered. The solid curve represents the probability that both nucleons in a $pN \rightarrow NN\pi$ scattering have momenta after the scattering which are not Pauli blocked. Only at the highest energies do two-pion reactions need to be introduced. This particular calculation represents a sharp Fermi sphere with radius 260 MeV/c and isotropic scattering, but small differences are obtained if a diffuse sphere of a Woods-Saxon type and/or nonisotropic scattering is introduced. The dashed curve includes also the possibility for reabsorption of the pion (as described in Sec. III D). Both curves are normalized to the data at 250 MeV beam energy. Even if reabsorption is introduced properly, one cannot expect agreement in the deep subthreshold region where collective phenomena play an important role. At higher energies where the increasing available phase space is important, it still appears as if the cross section increase is significantly larger. Before turning to detailed comparisons with a complete pion production model one should, however, remember that the increasing available phase space for pion production is a natural ingredient in nearly all such models, and definitely in the one we are to describe now.

B. Comparison to QMD calculations

Well-established microscopic—as well as mean-field $+NN$—models have been developed to describe the full dynamical evolution and the particle emission in both p-nucleus and nucleus-nucleus collisions. The Dubna cascade model [8] produces pions both in direct NN interactions and in two-step reactions including an intermediate Δ or off-shell nucleon. Good agreement between our $p+\mathrm{Ar}$ data and these calculations has been presented in Ref. [9]. The BUU model [10] was the first mean-field model that was introduced to describe pion production data. The dynamical evolution is here prescribed through equations that contain interaction with the mean field as well as with individual

nucleons (or rather test particles). It was shown in [7] that this model generally overpredicts the pion yield, particularly in the backward hemisphere, and it was suggested [7] that this discrepancy comes from the omission of the direct pion production channel and/or from the fact that no local, momentum-dependent NN potential has been introduced.

In this paper, we chose to compare the pion production data with molecular dynamics calculations [23], in which the direct production channels are introduced. The mean-field dynamics follows the nucleon molecular dynamics prescription in [24]. Nucleons are represented by Gaussian wave packets moving in a self-consistent mean-field potential according to the classical (Ehrenfest) equations of motion. The Hamiltonian of the interacting system is written as

$$H=\sum_{i=1}^{A}\frac{\vec{p}_i^{\,2}}{2m}+\frac{1}{2}\sum_{i=1}^{A}V_{Skyrme}(\vec{r}_i)+\frac{1}{2}\sum_{i=1}^{Z}\sum_{k=1,i\neq k}^{Z}\frac{e_1e_2}{|\vec{r}_i-\vec{r}_k|}, \tag{4}$$

with a Skyrme potential describing a soft equation of state:

$$V_{Skyrme}(\vec{r}_i)=-356\left(\frac{\rho(\vec{r}_i)}{\rho_0}\right)+303\left(\frac{\rho(\vec{r}_i)}{\rho_0}\right)^{7/6}. \tag{5}$$

Here A and Z are the nucleon and charge numbers of the nucleus, $\vec{p}_i$ and $\vec{r}_i$ are the individual nucleon momentum and position vectors, m is the nucleon mass, $e_{1,2}$ the charge (either e or 0), $\rho(\vec{r}_i)$ the local density, and ρ_0 the normal nuclear matter density (0.165 fm^{-3}). When two nucleons come to a relative distance closer than $\sqrt{\sigma_{eff}/\pi}$ they scatter and are given momentum vectors in the NN c.m. system according to an isotropic phase-space distribution. Pauli blocking prevents scattering of nucleons into already occupied phase space. All pions produced in direct NN collisions propagate in the mean Coulomb+nuclear potential of the surrounding nuclear matter. There they may be reabsorbed or rescattered in inverse πNN reactions with an energy-dependent mean free path (see Sec. III D).

Figure 6 presents the beam energy dependence of differential, $d\sigma/d\Omega$, π^+ cross sections. The $p+$Kr data in the beam energy region 300–400 MeV show smaller fluctuations in the data points and thus larger statistics. This comes from the part of the ramp with slower increase of the beam energy (see Sec. II A and Fig. 1) and reflects the demand from a search for narrow resonances which will be reported elsewhere. It should be noticed that the cross sections have been integrated over the pion energy region 16–75 MeV, for 90°, 120°, and 150°, over 11–84 MeV for 55° and 75°, and over 11–60 MeV for 20°.

Figure 7 shows the total integrated cross sections of π^+ from all four reactions that were studied. Extrapolations of cross sections below and above the region of detected pions are performed in the way described in Sec. III A. The QMD calculations describe the general tendency of the beam energy dependence quite well except at the lowest energies where the collective phenomena become important. It also appears, from the 150° $p+$Kr data (Fig. 6), as if the QMD calculations vastly underestimate the backward production of

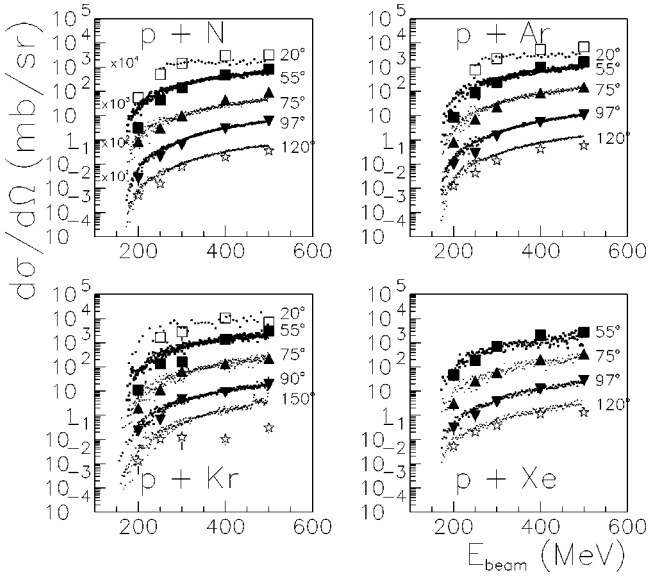

FIG. 6. Beam energy dependence of differential $(d\sigma/d\Omega)\pi^+$ cross sections in $p+A_t$ reactions. Large symbols represent molecular dynamics calculations. The slightly different pion energy intervals for the different angles are presented in the text.

pions. A careful investigation of the choice of the $NN\rightarrow NN+\pi$ angular distribution (here isotropic) and the choice of mean free path and dynamics for the reabsorption should, however, be made before further conclusions from this discrepancy can be made.

C. Target mass dependence

The (target) mass dependence on the total yield of π^+ is exploited in Fig. 8. Here τ is the exponent of an assumed

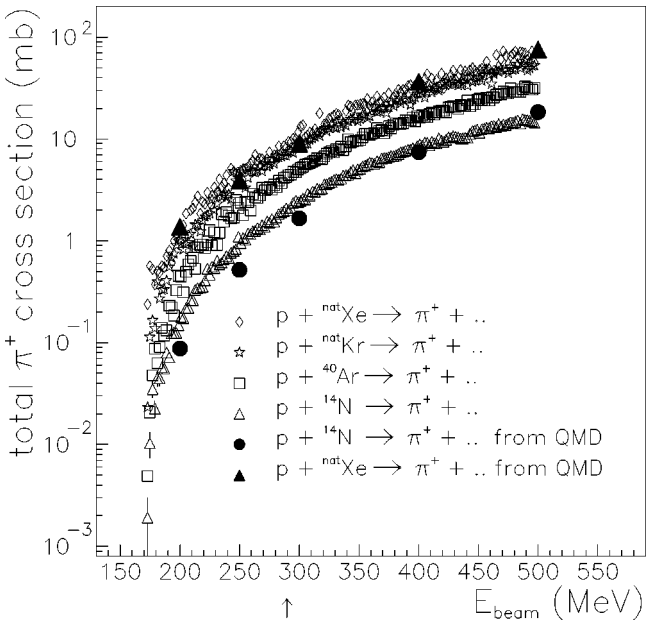

FIG. 7. The beam energy dependence of the total cross section of π^+ in $p+$N, $p+$Ar, $p+$Kr, and $p+$Xe reactions. The arrow marks the free $NN\rightarrow NN\pi$ threshold.

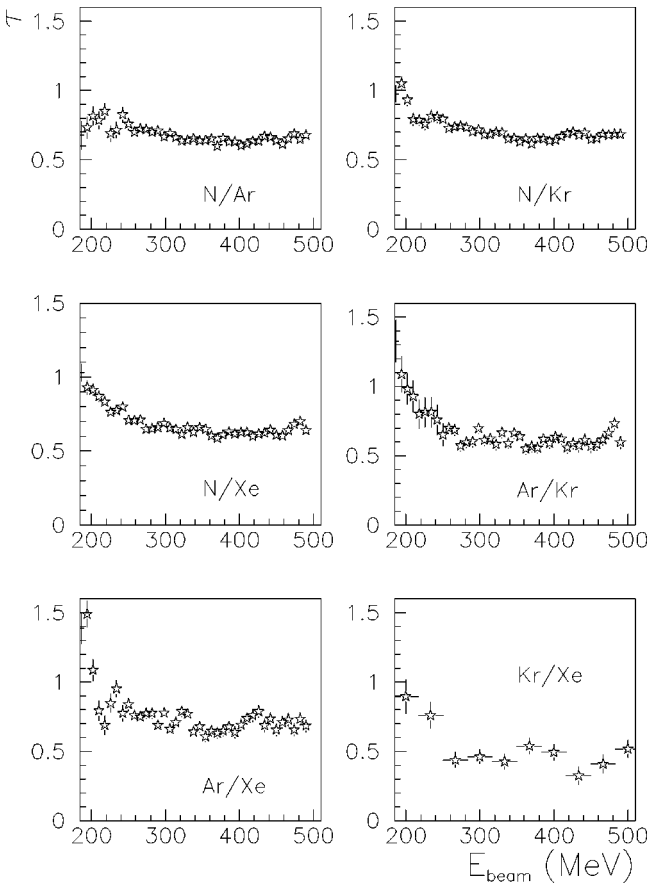

FIG. 8. The exponent τ (see text) as a function of the beam energy for six different target (X) combinations in $p+X$ reactions.

power law dependence $\sigma \sim A^{\tau}$. The mass dependence is stronger for light nuclei as observed earlier both in p-nucleus and nucleus-nucleus reactions [15].

Actually, τ is >1 at the lowest beam energies, $E_{beam} < 200$ MeV, because the difference in absolute threshold for different targets becomes important in this region. In the beam energy region where this effect is negligible, it appears as if τ decreases from 1 close to the threshold, naively indicating a strong collective (volume) effect in the pion production mechanism, to an asymptotic level varying between 1/2 for the heavy target nuclei to 2/3 or even more for light target nuclei (Table II).

The quality of these results is of course dependent on how well the extrapolation procedure (see Sec. III A) can be trusted. We therefore varied the set of parameters a, b, and c

TABLE II. The exponent τ for target mass dependence $\sigma \sim A^{\tau}$.

Cross section ratio	τ_{asympt}	τ_{250}	τ_{200}
N/Ar	0.68±0.05	0.70±0.08	0.80±0.09
N/Kr	0.70±0.05	0.83±0.08	0.97±0.09
N/Xe	0.62±0.05	0.74±0.07	0.95±0.07
Ar/Kr	0.61±0.06	0.73±0.07	1.08±0.07
Ar/Xe	0.70±0.07	0.90±0.08	1.1±0.1
Kr/Xe	0.40±0.1	0.60±0.15	0.95±0.20

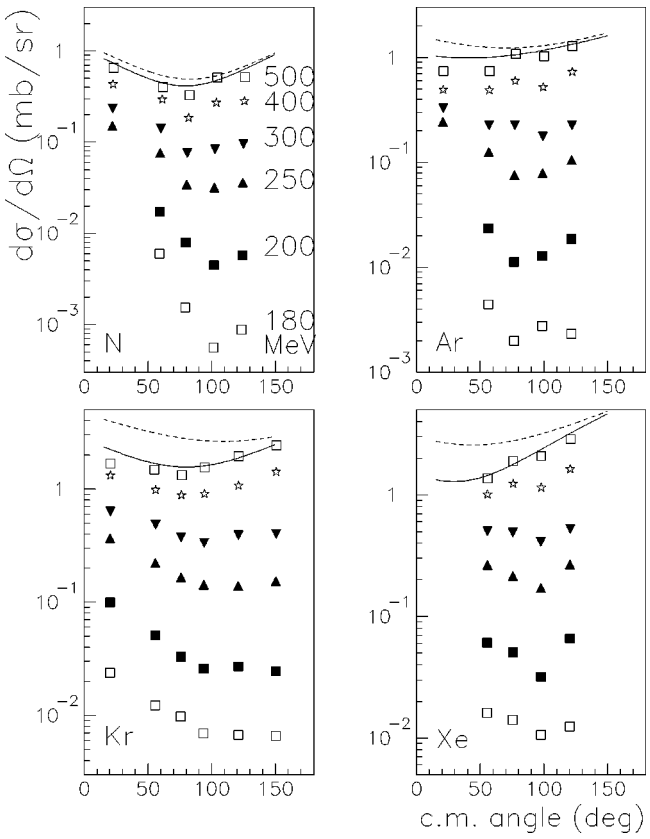

FIG. 9. Angular dependence of the emission of 18–64 MeV π^+ for different beam energies (labels in upper left figure). The target in the reaction is shown in the lower left corner. The solid curves are simple fits to the 500 MeV beam energy data and the dashed curves represent the distributions before reabsorption [26].

describing the angular dependence, within reasonable limits, and confirmed that this does not change our main conclusions. Thus there is a volume dependence—or at least a production process that simulates a volume dependence at low energies—which turns into a surfacelike behavior at higher energies. The fact that the black-disk behavior for the lighter nuclei is replaced by a peripheral behavior for heavier nuclei, $\tau \leqslant 1/2$, is probably essentially due to the increasing importance of the reabsorption of pions. A general conclusion in the energy region well above the threshold could thus be that a first-chance NN collision model with short mean free path for pions in nuclear matter may work well for light target nuclei but must be replaced by a complete NN scattering model of cascade type [25] or by mean-field prescriptions [10,23,24] when heavier targets are involved.

D. Angular distributions

The velocity of the system in which pions are emitted ranges from that of the (global) $p+A$ system to that of the NN system. The limited available pion energy region and the limited number of angular points in the data make presentations of angular distributions in systems with high velocity (or invariant cross section $p_{\parallel}-p_{\perp}$ contour plots) of little use. Therefore only angular distributions in the (global) $p+A$ system are presented in Fig. 9. It is important to notice that

the same pion energy interval, here 18–64 MeV, in the c.m. system is used in each case. For the forward (20°) telescope, an extrapolation has been introduced following the prescription in Sec. II E 2.

The following conclusions can be drawn.

(i) The forward peaking is quite strong at lower beam energies but this shifts to symmetric or even a slight backward peaking at high beam energies.

(ii) The backward emission exhibits a stronger beam energy dependence than the forward emission.

(iii) The forward/backward emission ratio is larger for the light target reactions at each beam energy.

As shown in Sec. III C, the QMD calculations can neither reproduce details in the angular distribution nor in the beam energy dependence close to threshold. Improvements can certainly be made in the choice of potentials, *NN* scattering distributions, and reabsorption processes. Apart from collective processes very close to threshold, the pion emission in a *p*-nucleus collision at low energies should be governed by the mean free path and the kinematics of the first *NN* scattering and the subsequent reabsorption of pions. An increasing role of the cascading will then appear with increasing beam energy. In order to sort out the reabsorption effect first, we performed calculations according to the prescription by Ericsson and Jakobsson [26]. There the production position is determined by the penetration of the proton from an energy-dependent *NN* mean free path combined with a Woods-Saxon density of the nucleus. Proper impact parameter weighting is of course also introduced. The pion then propagates inside the nucleus (in its rest system) and collides either elastically or inelastically (absorption) with probabilities given by mean free paths taken from optical calculations. In each angular distribution at 500 MeV the effect of reabsorption is shown by the curves in Fig. 9. It is thus obvious that the primary angular distributions (dashed curves), i.e., those before reabsorption, are rather independent of the target mass and have only weak forward peaking in the global c.m. system. This fact, plus the fact that the forward peaking gets more pronounced with decreasing beam energy, make the following general interpretations plausible:

The dominating part of the 18–64 MeV pions is produced in first-chance *NN* collisions in *p*-nucleus collisions even at energies of 500 MeV, i.e., substantially above the threshold. With decreasing beam energy a gradually increasing importance of collective, multinucleon, processes is observed. The decreasingly available phase space makes, however, the forward peaking of the pion emission increase.

E. π^- emission

The selection of π^- is made indirectly from the difference between the number of charged pions and the number of π^+. Therefore it depends critically on the resolution both in the $\Delta E-\Delta E$ correlations and the prompt-delayed ADC signal correlations (see Sec. II D). Only the second experiment ($p+\mathrm{Kr}$) had good enough resolution and only pions stopping in detectors 6–9 can be identified with high enough confidence, since normally several $\Delta E-\Delta E$ correlations are needed. This provides a pion energy interval of 44–70 MeV.

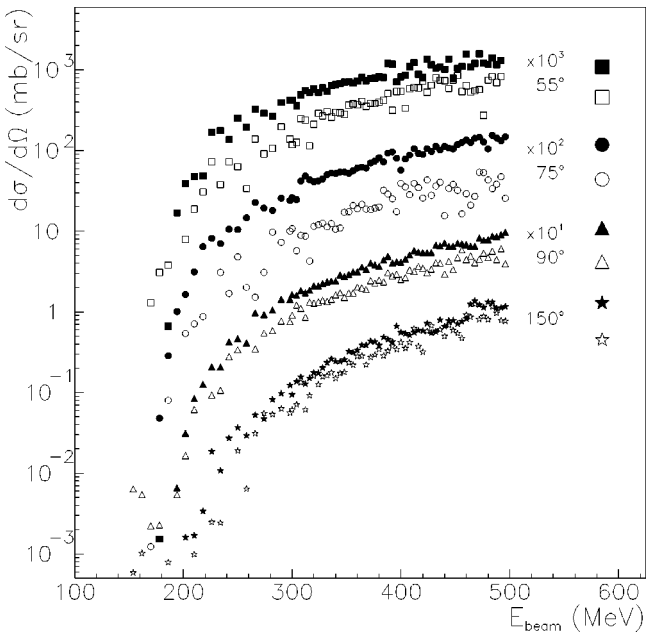

FIG. 10. The differential $d\sigma/d\Omega$ cross section as a function of beam energy for π^- (open symbols) and π^+ (solid symbols). The pion energy interval is 44–70 MeV. The large symbols refer to data from Ref. [3]

Differential cross sections for these π^- are presented in Fig. 10 together with the corresponding π^+ cross sections.

Comparisons can be made to the time-of-flight spectrometer data of Crawford *et al.* [3] at 585 MeV (large symbols) after integrating these double differential, $d^2\sigma/d\Omega dE$, cross sections over 44–70 MeV pion energy and interpolating the mass and charge dependence of the target. Statistical errors are in both cases small but the systematic errors are quite large in our π^- data (40–60 %) while they should be of the order of 20–30 % in the data of Crawford *et al.* In view of this, the agreement between our data and those of Ref. [3] is quite acceptable.

Figure 11 shows the N_{π^+}/N_{π^-} ratio for pions in this restricted energy interval, 44–70 MeV, as a function of the beam energy. The solid histogram represents the yield in the directly measured 55°–150° angular region while the dashed histogram includes interpolations and extrapolations of the angular distribution (Sec. III A) to obtain the total angle integrated yield. Both points at 585 MeV are extracted from the data of Ref. [3], and since no important beam energy dependence of π^+/π^- is expected between 500 MeV and 585 MeV, it appears as if the π^+ excess is somewhat larger in the data of Crawford *et al.*

A direct estimate of the total yield ratio, from *NN* scattering decomposed into different isospin components, gives

$$\frac{N_{\pi^+}}{N_{\pi^-}}=\frac{\frac{Z_t}{A_t}[\sigma_{01}+\sigma_{01}(d)+\sigma_{11}]+\frac{1}{2}\frac{(A_t-Z_t)}{A_t}(\sigma_{01}+\sigma_{11})}{\frac{1}{2}\frac{(A_t-Z_t)}{A_t}(\sigma_{01}+\sigma_{11})}. \tag{6}$$

Here σ_{01} stands for one neutron and one proton in the

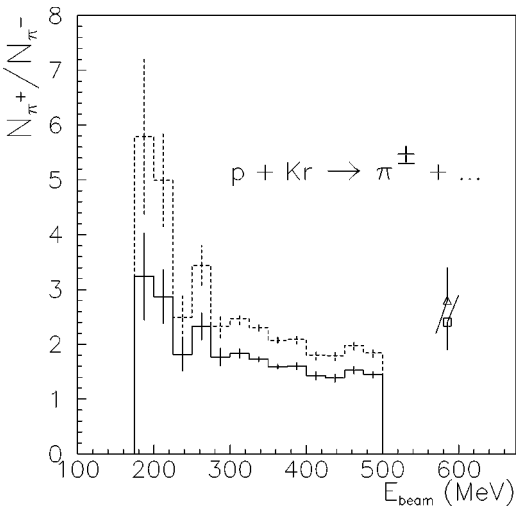

FIG. 11. N_{π^+}/N_{π^-} ratios of the yield in the 44–70 MeV pion energy interval as a function of the beam energy. The points at 585 MeV are from Ref. [3]. The solid histogram and the lower point represent the 55°–150° data, and the dashed histogram and upper point represent the total angle integrated yields.

final state while the $\sigma_{01}(d)$ is the corresponding bound deuteron state. The $\sigma_{01}(d)$ is dominating only very close to threshold [27] where the N_{π^+}/N_{π^-} ratio would approach infinity according to Eq. (6). The combination of large statistical errors and large systematic errors in the threshold region makes, however, any comparison, say, below 300 MeV, of limited value. In the 300–500 MeV region where errors are reasonably small one may instead use the approximation $\sigma_{01}(d) \approx \sigma_{01}$ and neglect the σ_{11} component, which gives $N_{\pi^+}/N_{\pi^-} \approx 4Z/(A-Z)+1$, and thus gives a ratio of 4.5 for $p+\mathrm{Kr}$. At even higher beam energies the $\sigma_{01}(d)$ component could be neglected and there the N_{π^+}/N_{π^-} ratio would approach 2.5.

Our data thus exhibit a small N_{π^+}/N_{π^-} ratio as compared to the simple first-chance *NN* scattering prescription, but it should be stressed that the 585 MeV data [3] show that the π^+/π^- ratio is substantially smaller in the 44–70 MeV region than that for the total pion yield. The effect of the pion interaction with the Coulomb field is obvious. The energy shifts in opposite ways for π^+ and π^-, in combination with, e.g., a Boltzmann + exponential distribution has a delicate impact on the π^+ to π^- ratio. This is explored very clearly in [3] where it is shown that the 44–70 MeV region for π^- falls on either the increasing side of the energy distribution or the decreasing side, depending on the emission angle. The corresponding π^+ region falls instead always on the exponentially decreasing side. The cascade approach [9] does reproduce our π^+/π^- ratio data well whereas in the QMD approach some difficulties with this are observed. Any model for *p*-nucleus reactions, claiming to reproduce details of these π^+/π^- ratios, must obviously include both the time-dependent Coulomb field and the absorption process of both π^+ and π^- properly.

IV. CONCLUSIONS

Excitation function data of π^+ production in p-nucleus collisions from the absolute threshold to 500 MeV, i.e., to the region dominated by Δ excitation, have been presented. Continuous data taking during slow ramping of a stored beam that interacts with an ultrathin gas-jet target is proved to be possible.

The target mass dependence evolves from $\sim A_t^1$ to $\sim A_t^{2/3}$ or even $\sim A_t^{1/2}$ for heavy targets when increasing the beam energy. This indicates a gradual development from a volume like (pionic fusion) mechanism to a surfacelike (individual *NN* scattering) mechanism. In addition details in the target mass dependence show that reabsorption plays an important role, especially for heavy targets.

The beam energy dependence of the cross sections is reasonably well described by QMD calculations except for details in the forward/backward production ratios, and an obvious difficulty in dealing with the collective processes at the lowest beam energies, very close to the absolute threshold.

The π^+/π^- ratio in the limited energy interval 44–70 MeV deviates strongly from the simple prescription of isospin decomposition of *NN* scattering. It is suggested that this is mainly caused by the interaction of the pions with the Coulomb field.

ACKNOWLEDGMENTS

The authors thank the accelerator staff of the The Svedberg Laboratory for its excellent technical support and the Swedish Natural Science Research Council for its financial support.

[1] E. Fermi, Phys. Rev. **92**, 452 (1953).
[2] M. M. Sternheim and R. R. Silbar, Phys. Rev. D **6**, 3117 (1972).
[3] J. F. Crawford *et al.*, Phys. Rev. C **22**, 1184 (1980).
[4] C. Ellegaard *et al.*, Phys. Lett. **50**, 1745 (1983).
[5] H. Oeschler, Technische University Darmstadt Report No. IKDA 98/20, 1998.
[6] W. Cassing, V. Metag, U. Mosel, and K. Niita, Phys. Rep. **188**, 363 (1988).
[7] B. Jakobsson *et al.*, Phys. Rev. Lett. **78**, 3828 (1997).
[8] K. K. Gudima, H. Iwe, and V. D. Toneev, J. Phys. G **5**, 229 (1979).
[9] K. K. Gudima and M. Ploszajczak, GANIL Report No. P9817, 1998.
[10] B. Li and W. Bauer, Phys. Rev. C **44**, 450 (1991); B. Li, W. Bauer, and G. F. Bertsch, *ibid.* **44**, 2095 (1991).
[11] T. Bergmark *et al.*, in TSL Progress Report 1987–1991, p. 19, and 1992–1993, p. 14; L-O. Andersson *et al.*, in TSL Progress Report 1994–1995, p. 12, edited by A. Ingemarsson.
[12] C. Ekström, in *Proceedings of the 19th International Symposium on Cooler Rings and their Applications*, Tokyo, 1990, edited by T. Katayama and A. Noda (World Scientific, Singapore, 1991), p. 228.
[13] V. A. Krasnov, A. B. Kurepin, A. I. Reshetin, K. O. Oganes-

jan, and E. A. Pasyuk, Phys. Lett. **108B**, 11 (1982).
[14] J. Julien *et al.*, Z. Phys. A **347**, 181 (1994).
[15] B. Norén *et al.*, Nucl. Phys. **A489**, 763 (1988).
[16] T. Johansson *et al.*, Phys. Rev. Lett. **48**, 732 (1982).
[17] V. Bernard *et al.*, Nucl. Phys. **A423**, 511 (1984).
[18] W. A. Richter *et al.*, Phys. Rev. C **49**, 1001 (1994).
[19] A. A. Cowley *et al.*, Phys. Rev. C **43**, 678 (1991).
[20] J. Chiba, Ph.D. thesis, University of Tokyo, Report No. UTPN 130, 1979.
[21] G. Sanouillet *et al.*, CEN Saclay Internal Report No. CEA-N-2483, 1986.
[22] B. Million (private communication); B. Jakobsson, Phys. Scr. **48**, 179 (1993) and references therein.
[23] A. Fokin, Ph.D. thesis, Lund University, 1998.
[24] J. P. Bondorf, D. Idier, and I. Mishustin, Phys. Lett. B **359**, 261 (1995).
[25] J. Cugnon, T. Mizutani, and J. Vandermeulen, Nucl. Phys. **A352**, 505 (1981).
[26] G. Ericsson and B. Jakobsson, in *Proceedings of the First European Biennial Workshop on Nuclear Physics*, Megéve, 1991, edited by D. Guinet and J. R. Pizzi (World Scientific, Singapore, 1991), p. 200.
[27] J. Lock and D. F. Measday, *Intermediate Energy Nuclear Physics* (Methuen, London, 1970).